Full paper

All-in-one piezoresistive-sensing patch integrated with micro-supercapacitor

Yu Song[a], Haotian Chen[a,b], Xuexian Chen[a,b], Hanxiang Wu[a], Hang Guo[a,b], Xiaoliang Cheng[a], Bo Meng[a], Haixia Zhang[a,b,*]

[a] National Key Laboratory of Science and Technology on Micro/Nano Fabrication, Peking University, Beijing 100871, China
[b] Academy for Advanced Interdisciplinary Studies, Peking University, Beijing 100871, China

ARTICLE INFO

ABSTRACT

Portable and wearable sensors have attracted considerable attention, which could perceive and respond to ambient stimuli accurately. For the sake of solving the limited power supply and low integration, it is critical to develop and combine functional electronics with flexible energy devices. In this work, we designed an all-in-one sensing patch integrated with piezoresistance sensor and micro-supercapacitor with the porous CNT-PDMS elastomer. Taking the advantage of porous structure with piezoresistivity and elastomer with electrochemical performance, the piezoresistance sensor shows high sensitivity ($0.51\,\mathrm{kPa^{-1}}$) and wide detection range as functional fraction, and micro-supercapacitor maintains excellent areal capacitance and cycling stability after 6000 cycles as energy storage fraction, respectively. Assembled with piezoresistance sensor and micro-supercapacitor, the sensing patch could be easily attached on the epidermal skin for joint and muscle monitor with the corresponding resistance response. With high sensitivity and mechanical robustness, such sensing patch could be further utilized as a 3D touch in user identification and safety communication through feature parameter extraction and signal decoding. After packaged into the sensing patch matrix, it could be achieved for static pressure sensing and dynamic tactile trajectory. Therefore, the all-in-one sensing patch shows feasibility in real-time pressure recognition and human-machine interfaces.

1. Introduction

Recently, the demands for flexible, smart and integrated electronics have dramatically grown due to the increasing interest in wearable and portable devices, ranging from medical diagnosis [1], epidermal health monitor [2] to safety communication [3], *etc*. Research about developing smart energy system has been extensively investigated with the fruitful material synthesis and fabrication promotion [4,5]. Smart energy system includes three components: energy harvesting fraction, such as triboelectric nanogenerator and piezoelectric nanogenerator [6–8]; energy storage fraction, such as supercapacitor and Li-ion battery [9–11]; and functional fraction, such as strain sensor, humidity sensor [12–14], respectively. Confronted with body-attachable monitor and human-machine interfaces, multi-sensors with energy storage devices on a deformable substrate with stable functions and integrated configuration will be essential for the realization of smart energy systems [15–17].

In order to meet the demands for monitoring human activities, intensive efforts have been devoted to developing flexible pressure-sensitive sensors. Numerous sensors have been realized by utilizing triboelectric [18], piezoresistance [19] and capacitive effects [20], while piezoresistance sensors (PRSs) exhibit ideal characteristics [21–23]. By transducing the external pressure into resistance signal, PRSs are expected to possess wide dynamic strain ranges, high sensitivity, stability and compatibility. Considering the fact that conventional PRS with conductive polymer films or elastomeric rubbers lacks in sensitivity and mass fabrication [24,25], porous structure is introduced with the combination of elastomeric piezoresistance nanocomposites and conductive nanomaterials to enhance the sensitivity of PRS for epidermal application [26,27]. To achieve the electrical conductivity and mechanical property at the same time, such conductive porous structure are considered as the optimal candidate owing to their synergistic effect of high conductivity of active materials and excellent mechanical robustness of the porous scaffold [28]. The capability of the PRS could be further modulated by the pore structure and percolation transport between adjacent conductive materials, which performs high sensitivity and low strain detecting capability [29]. Such attachable sensors are strongly dependent on the power supply, however, it is impractical to operate devices via long wires connected and external power supply in wearable technologies. Therefore, integrating PRS with

---

energy storage devices is an effective strategy to accomplish a self-driving system for specific wearable applications.

Among various energy storage devices, supercapacitor is a promising device due to their cycling stability and biocompatibility [30]. Unfortunately, conventional supercapacitor with sandwiched structure limits its application in on-chip devices and microsystems, because the miniaturized electronics requires energy component with similar dimension compared with other elements. Nowadays, the in-planar supercapacitor, also called micro-supercapacitor (MSC) [31–33], has drawn tremendous attentions in micro energy fields. Owing to the in-planar layout and elimination of separator, the total thickness of the device could be greatly reduced, which maintains excellent electrochemical performance and satisfies integration at the same time [34]. According to previous studies, researchers have made considerable contributions to enhancing the energy density and reliability of the MSC by utilizing different active nanomaterials and developing advanced structure [35]. On the one hand, carbon-based materials such as carbon nanotubes (CNTs), graphene and activated carbons have been widely discussed [36]. On the other hand, solid-state electrolytes are employed, which could broaden the applications of the MSC with flexibility in wearable devices [37]. Most of the works mainly focused on the performance improvement, but ignored the cost, ease of fabrication and device integration. To avoid the complicated fabrication with lithography process and transfer approach, it is essential to develop MSC with high conductive active materials and controllable interdigital pattern.

In this work, we propose an all-in-one sensing patch integrated with PRS and MSC based on the porous carbon nanotube-polydimethylsiloxane (CNT-PDMS) elastomer. With facile and novel approach, the porous CNT-PDMS elastomer is synthesized through solution-evaporation method with the help of sugar templates. The mechanical durability and electrical stability of the porous CNT-PDMS elastomer could be modulated by the CNT content and sugar template size, which plays a fundamental role in smart energy systems. As the functional fraction, the PRS demonstrates remarkable piezoresistance performance with high sensitivity and wide range of deformations. The resistance response shows good reliability under repeated applied stress and reflects compressive strain accurately. Through laser patterning and electrolyte transferring process, the MSC could be developed with porous CNT-PDMS elastomer as active materials and solid-state electrolyte as both flexible substrate and ion reservoir. Taking advantage of high conductivity and large surface area, the entire device shows reliable electrochemical performance and cycling stability. By assembling the PRS with MSC, an all-in-one sensing patch could be attached to the epidermal skin, showing versatile capabilities in monitoring human joint and muscle movements. In addition, the piezoresistive-sensing patch with high sensitivity and mechanical robustness has potential applications in user identification and safety communication through the feature parameter extraction and decoding as the 3D touch. Packaged into the sensing matrix, sensing patch units show feasibility in spatially mapping resolved pressure information about static pressure sensing and dynamic tactile trajectory. Therefore, assisted by the all-in-one high integration structure, piezoresistive-sensing patch has a broad prospective in widespread applications and lays a solid foundation toward the realization of advanced electronics and smart energy systems.

2. Experimental

2.1. Fabrication of CNT-PDMS elastomer

CNT-PDMS elastomer is produced by the solution-evaporation method. As we know, it is difficult to disperse CNTs uniformly within the PDMS matrix if they are directly mixed, as individual CNTs tend to agglomerate together in a viscous fluid. Wetting dry CNT powder in solvent with PDMS is a possible approach to improve the dispersion of CNTs in the PDMS matrix [38]. In detail, a toluene solvent is used to disperse CNTs with PDMS matrix homogeneously at the volume ratio of 5:1. Firstly, multi-walled CNTs (diameter: 10–20 nm, length: 10–30 μm, purity > 98%, Boyu Co.) are dispersed in toluene solvent with PDMS base resin (Sylgard 184, Dow Corning Co, USA) and the mixture is magnetic stirred for 4 h at room temperature. Then the mixture is poured into a culture dish after CNTs are mixed into PDMS thoroughly with the help of toluene. Subsequently, the curing agent is added to the CNT-PDMS liquid at a ratio of 1:10 with magnetic stirring until the toluene is entirely evaporated. Finally, the CNT-PDMS elastomer could be prepared after the whole mixture is baked on the hot plate at 120 °C for one hour.

2.2. Fabrication of porous CNT-PDMS elastomer

The porous CNT-PDMS elastomer assisted by the sugar template is made using 3D soft lithography. Various sizes of sugar templates are developed by controlling the grinding time of sanding sugar. By adding them into CNT-PDMS liquid at the weight ratio of 4:1, the total mixture is magnetically stirred to evaporate residual toluene. Degassed in a vacuum chamber, the sugar templates with the absorbed mixture are then cured at 110 °C for 20 min with the help of curing agent at a ratio of 1:10. After the curing process, the sugar templates are dissolved completely and washed away by soaking them in an ultrasonic cleaner at 40 °C before drying in air. Finally, after the removal of the sugar templates, 3D interconnected porous CNT-PDMS elastomers are produced.

2.3. Fabrication of the all-on-one sensing patch

All-in-one sensing patch is integrated with PRS and MSC with bottom-up structure. For the PRS, the prepared CNT-PDMS-sugar mixture is poured into flat, enclosed mold with designed size. After the curing-dissolution process mentioned above, the PRS is developed as the functional fraction. As for the MSC, we combine laser patterning with electrolyte transferring process based on the porous CNT-PDMS elastomer. Such in-planar and electrolyte-substrate layout could improve device integration and attachment greatly. Through PDMS membrane adhesion, both the PRS and MSC could be easily assembled on both sides to realize the all-in-one sensing patch.

2.4. Characterization and measurement

Morphologies of the sugar, porous structure and MSC is observed using Scanning electron microscopy (SEM, Quanta 600F, FEI Co.) with an operation voltage of 5 kV. Mechanical measurements of the porous CNT-PDMS elastomer are carried out using a push-pull gauge (Handpi Co.). For the electrical analysis, the voltage of the PRS is amplified by a SR560 low-noise voltage amplifier from Stanford Research Systems and measured via a digital oscilloscope (Agilent DSO-X 2014A). Additionally, the performance of the MSC is evaluated through CHI660 electrochemical workstation (Chenghua Co.) with a two-electrode configuration. Water contact angle is recorded by the measurement system (OCA 30, Data Physics Instruments GmbH).

3. Results and discussion

3.1. Design of the all-in-one sensing patch

The system of all-in-one patch for pressure sensing is schematically illustrated in Fig. 1, which consists of two parts: piezoresistance sensor as functional fraction and micro-supercapacitor as energy storage fraction. As shown in Fig. 1a, both components are integrated on the PDMS substrate based on the porous CNT-PDMS elastomer. The circuit diagram introduces the working principle of the sensing patch, where the charged MSC could drive the PRS effectively to monitor ambient pressure. Fig. 1b demonstrates the fabrication process of the porous
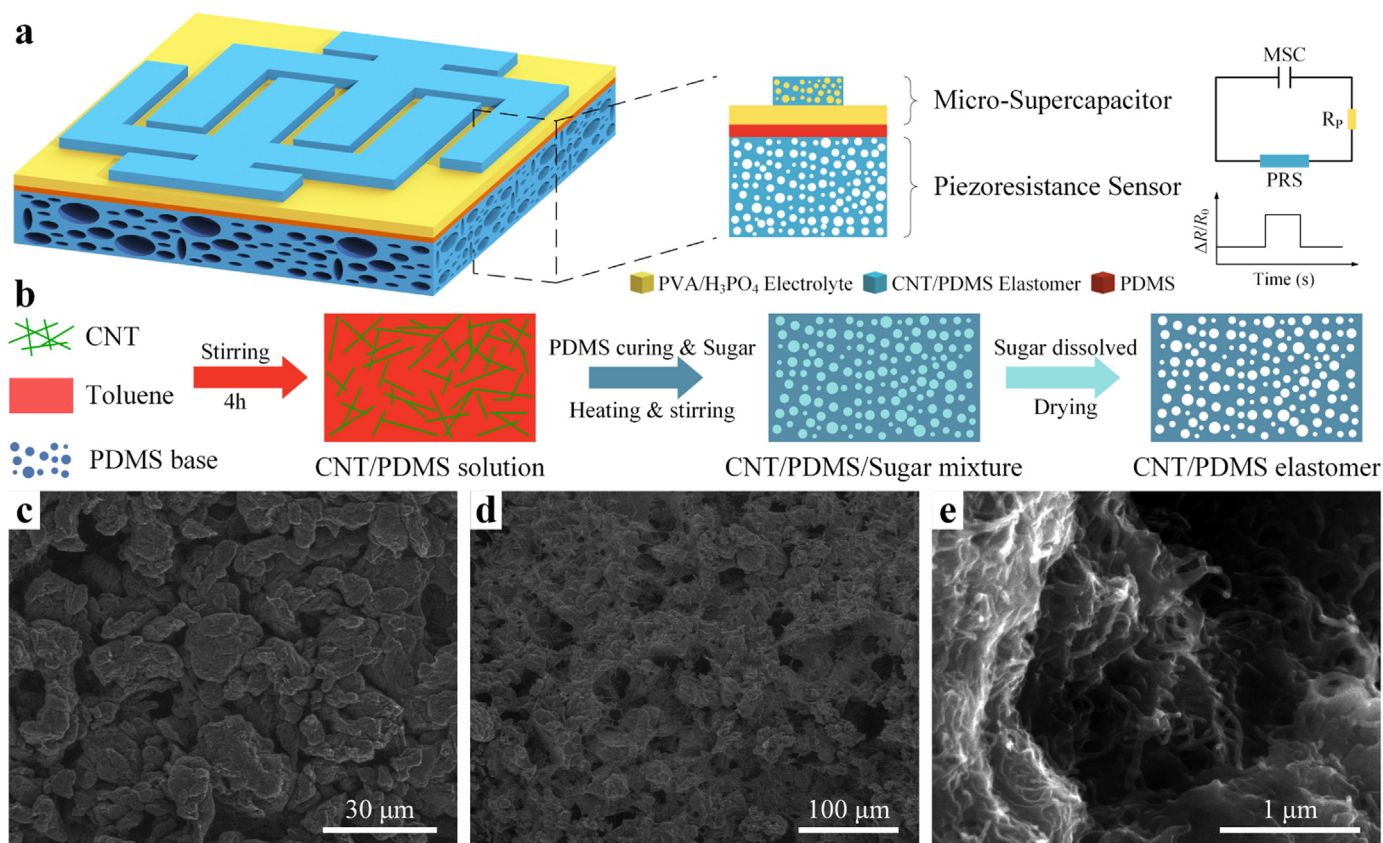
Fig. 1. a) Schematic illustration of all-in-one sensing patch integrated with piezoresistance sensor and micro-supercapacitor based on the porous CNT-PDMS elastomer. b) Fabrication of porous CNT-PDMS elastomer with solution-evaporation method assisted by sugar templates. SEM images of morphology of c) CNT-PDMS-sugar mixture, and porous CNT-PDMS elastomer d) after sugar dissolving e) with exposed CNTs.

CNT-PDMS elastomer through the solution-evaporation method. With the help of toluene solvent, CNT could be dispersed evenly with the PDMS base under the vigorous stirring. By adding the curing agent and sugar templates, the CNT-PDMS-sugar mixture could be prepared with the complete evaporation of residual toluene. After the sugar is dissolved in the water, the porous CNT-PDMS elastomer could be successfully developed.

SEM image in Fig. 1c shows the morphology of CNT-PDMS-sugar mixture with uniform sugar size. After the sugar is dissolved, the SEM image in Fig. 1d illustrates the CNT-PDMS elastomer possesses an open network of pore with large surface area. The enlarged SEM image of the porous scaffold proves that CNTs are exposed beyond the surface, which could efficiently form the conductive network. (Fig. 1e). Additionally, SEM images of sugar templates with different size and their corresponding porous structure are shown in the Fig. S1 in the Supporting information. Definitely, the mechanical performance of the CNT-PDMS elastomer is related to the porous structure (porosity, pore size) [26], and the electrical conductivity of the CNT-PDMS elastomer is influenced by the CNT content, respectively. Therefore, CNT-PDMS elastomer could be modulated by the content of additive (CNT, sugar template) and sugar size, showing suitable candidates as specific component in various devices. Under the same porous structure, the initial resistance of CNT-PDMS elastomers with different CNT contents is shown in Fig. S2 (Supporting information), showing that the percolation value (N_C) is around 2.5 wt% of CNT content. After the conductive path is formed, the resistance decreases sharply with the increase of CNT content. Additionally, the percolation value is strongly dependent on the diameter of CNT, which could be proved according to the Table S1 in the Supporting information.

### 3.2. Mechanical and electrical performance of the piezoresistance sensor

Firstly, to validate the tolerance of the fabricated PRS under external stimuli, such as physical vibration and ambient pressure, iterative compression tests of PRSs with different width, thickness and pore size under maximum strain of 60% are performed using the universal push-pull gauge (Fig. S3, Supporting information). The typical compressing process of the porous structure could be briefly divided into two distinct parts as shown in Fig. 2a–c. In the first stage called plateau region, the wall of the porous cell bends and collapses. With the strain increasing, it comes to the second stage, where the cell is collapsed sufficiently and further compressed. In this densification region, most of the air has been squeezed out and cell walls have been stacked together and behave like bulk materials. Apparently, the Young's modulus is almost the same with rigid material. While in the releasing process, the curve almost returns to the origin without plastic deformation, indicating that porous CNT-PDMS elastomer could tolerate the large deformation of mechanical strength.

An ideal honeycomb model is adopted as the basic cell, and Young's modulus corresponding to these two stages could be calculated as follows:

$$E_1 = 0.22(\frac{t}{b})^3 E_S \tag{1}$$

$$E_2 \approx E_S \tag{2}$$

where E_S is the Young's modulus of the bulk material, b and t are the length and thickness of the cell wall, respectively. Detailed model parameters and calculation process have been discussed in Fig. S3 (Supporting information).
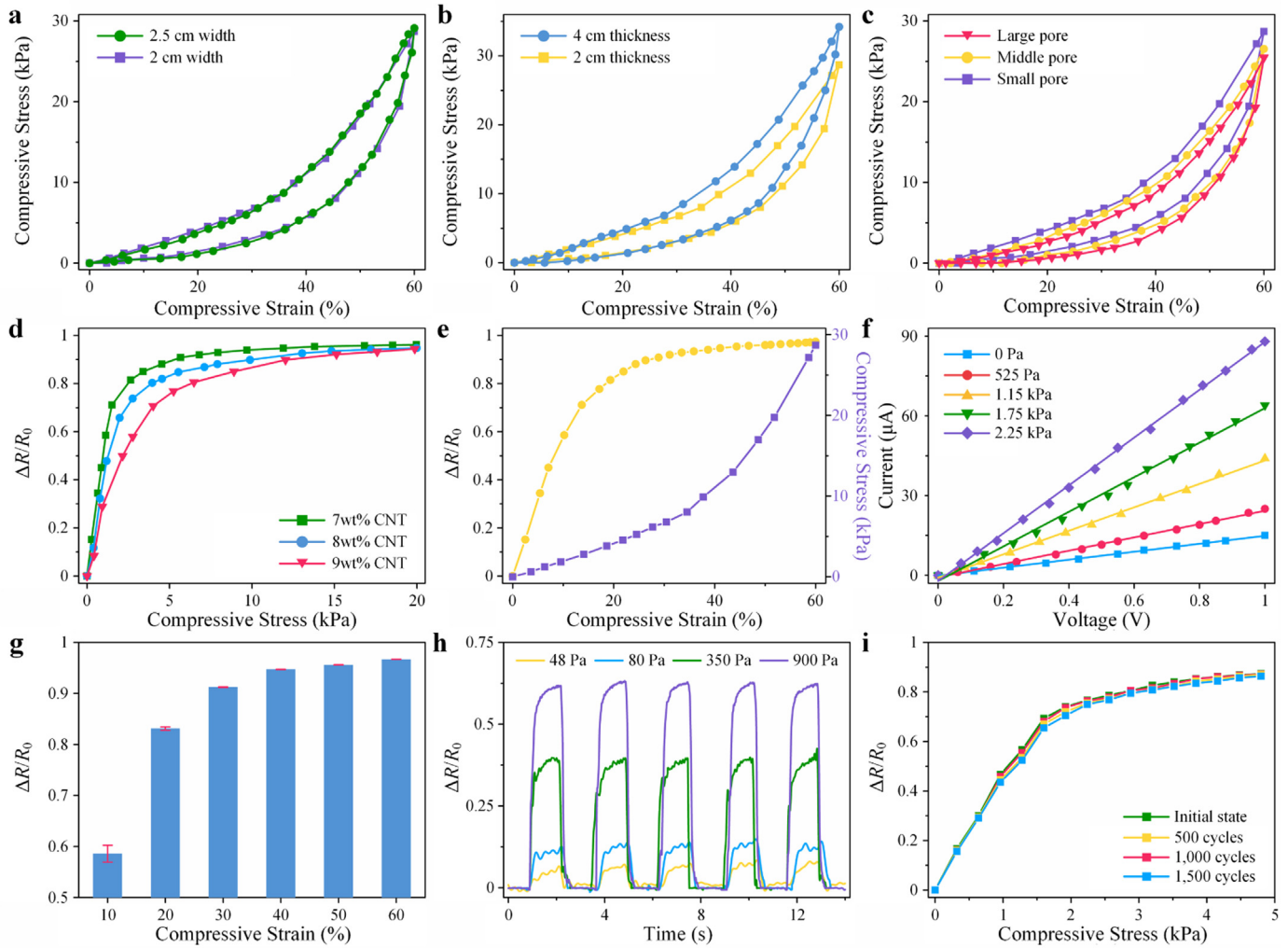
Fig. 2. a–c) The stress-strain curves of porous CNT-PDMS elastomer at maximum strain of 60% with different width, thickness and pore size. d) Resistance responses of assembled PRS with different CNT contents under different stress. e) The relationship of resistance response and stress with compressive strain. f) Current-voltage (*I-V*) curves of PRS under various stress. g) Resistance response variation with different compressive strain. h) Resistance response of repeated compressing-releasing cycles with different stress. i) Resistance response performance before and after 1500 cycles of compressing-releasing process.

It could be observed that Young's modulus is irrelevant to the device dimension such as width and thickness. Through the mechanical tests, the PRSs with different width own similar stress-strain curves (Fig. 2a) while the thicker device is more rigid and resistant to the compression (Fig. 2b). When PRSs are introduced with different pore size (*b*), Fig. 2c implies that PRS with larger pore size owns more elastic modulus gradient in the plateau region, which is consistent with the Eq. (1) where the larger *b* leads to the smaller Young's modulus. To maintain the reliability and mechanical robustness, PRS with width of 2.5 cm, thickness of 2 mm and small pore size of 20 μm is utilized for further test and discussion.

Then to evaluate the relationship of the mechanical and piezo-resistance performance, the resistance response of PRS is recorded under the compressing process. According to the formula of resistance:

$$R = \rho \frac{L}{A} \tag{3}$$

where *R* is the vertical resistance of the device, *L* is the vertical length, *A* is the cross section area and ρ is the resistivity, respectively. For the porous structure, both the decreased cross section area and increased length contribute to large resistance compared to the flat film. Additionally, the resistivity depends on the CNT content, where lower CNT content leads to higher resistivity. The resistance response (ΔR/R)

could be described as:

$$\Delta R/R = \Delta L/L + \Delta \rho/\rho - \Delta A/A \tag{4}$$

To characterize the performance of the PRS response, sensitivity (*S*) is defined as follows:

$$S = \frac{\Delta(\Delta R/R)}{\Delta \sigma} = \frac{\Delta(\Delta L/L)}{\Delta \sigma} + \frac{\Delta(\Delta \rho/\rho)}{\Delta \sigma} - \frac{\Delta(\Delta A/A)}{\Delta \sigma} \tag{5}$$

where σ is the stress applied on the PRS, According to the definition of Young's modulus:

$$E = \frac{\Delta \sigma}{\Delta \varepsilon} = \frac{\Delta \sigma}{\Delta(\Delta L/L)} \tag{6}$$

where ε represents the compressive strain and the first term of Eq. (5) can be expressed as $\frac{1}{E}$. From the analyzation of the percolation theory [29], the second term of the Eq. (5) is dependent on the CNT content with the relationship of:

$$\Delta \rho/\rho \propto (N - N_C)^{-n_\varepsilon} \tag{7}$$

where *N* is the CNT content, N_C is the percolation threshold of CNT content which could exactly form the conductive network and n_ε is the factor associated with the geometrical feature, respectively. According to the calculation in the Fig. S3 (Supporting information), Poisson's

ratio (ν) equals to 1, where the cross section area of the porous structure is almost unchanged ($\Delta A \approx 0$) during the compressing process. The sensitivity could be further described as:

$$S \propto \frac{1}{E} + \frac{k \cdot (N - N_C)^{-n_\varepsilon}}{\Delta \sigma} \tag{8}$$

where k is the coefficient factor to reflect the relationship between the resistivity and the CNT content.

Assisted by the analysis above, the sensitivity of the PRS is attributed to the Young's modulus and CNT content together. On one hand, for the uniform CNT content, small Young's modulus of porous structure is more sensitive to the applied stress. On the other hand, when the size of the porous device is determined, relatively low CNT content leads in the higher sensitivity definitely.

Fig. 2d demonstrates the resistance response curve of three PRSs with different CNT contents under the same pore structure, the slope of which represents the sensitivity. It could be observed that when the CNT content is higher than the percolation threshold, increased CNTs will decrease the resistivity and further reduce its sensitivity. Apparently, this resistance response trend is consistent to the theoretical analysis.

Meanwhile, it should be noted that lower CNT content aggravates the possibility of open circuit and higher sensitivity would narrow the measurement range. Thus, PRS with 7% CNT content and small pore size is optimal candidate, which maintains high sensitivity and mechanical robustness at the same time. In detail, the resistance response shows a linear increase against compressive stress in the first 0–2 kPa range, exhibiting a great sensitivity of $0.51\,\text{kPa}^{-1}$ shown in Fig. S4 (Supporting information).

Besides, gauge factor (*GF*) is another means to evaluate the performance of PRS, which could be defined as follows:

$$GF = \frac{\Delta R/R}{\varepsilon} = \frac{\Delta \rho / \rho}{\varepsilon} + 1 + 2\nu \tag{9}$$

where ν means the Poisson's ratio. The resistance response curves of PRSs with different CNT contents under the same compressive strain have been shown in the Fig. S3d (Supporting information). Combined with the analysis mentioned above, it could be concluded that gauge factor owns the positive correlation trend with the sensitivity. Then for the chosen PRS, the stress-strain curve and gauge factor curve are depicted in Fig. 2e. Two distinctive ranges could be observed, which correspond to the two compression regions. In the plateau region, the effective Young's modulus is relatively small, which brings in higher gauge factor and sensitivity. As the porous CNT-PDMS elastomer continues to be compressed into densification region, the Young's modulus increases to the original value, leading to the decrease of gauge factor and sensitivity. Therefore, the mechanical performance is strongly related to the piezoresistance behavior of the PRS device through both theoretical analysis and experimental verification.

As for overall measurements of the presented PRS, we measure the resistance responses to different stress applied among the device. The current-voltage (*I-V*) characteristics of PRS under different stress indicate that the response of device is quite reliable. *I-V* curve displays good linear behavior, the slope of which maintains constant under each applied stress. The resistance response could be obtained under repeated compressive strains from 10% to 60% (Fig. 2g). Large strain will enhance resistance response intensity, which is quite stable under the same strain condition. Fig. 2h shows representative resistance responses of PRS to repeated compressing and releasing cycles. Low stress could be detected and reliable resistance responses are observed at four different stress. Furthermore, after repeated bending for over 1500 cycles, the performance of the device shows negligible variation (Fig. 2i) under the same stress region with mechanical durability.

As for the stability of the device, the initial resistance is quite steady in the first 500 compressing-releasing process cycles shown in Fig. S3e (Supporting information). Furthermore, Table S2 in the Supporting

information compares the sensitivity and detection range of our device with other reported researches [17,27,39–42]. Along with the enhanced sensitivity, other performance of PRS has not been influenced. For the response capability, the applied stress could be responded by the PRS immediately with the fast response time of 22 ms (rise time) and 80 ms (release time), which could be utilized as the real-time health monitor of wearable devices (Fig. S3f, Supporting information).

3.3. Electrochemical analysis of the micro-supercapacitor

Then for the energy storage fraction, the flexible MSC is fabricated through laser-patterning and electrolyte-transferring process with prepared porous CNT-PDMS elastomer shown in Fig. 3a. Configured with the in-planar and electrolyte-substrate layout, the thickness of the MSC could be greatly decreased. The flexibility and portability of the device could improve its integration capability with other functional devices. Detailed fabrication process is illustrated in Fig. S5 (Supporting information). Obviously, the MSC owns a well-defined shape, which could be easily rolled up and meet the demands in portable electronics. The Fig. S6 (Supporting information) includes the parameter of each symbol, where MSC unit owns uniform interdigital finger. The SEM image of cross-sectional of the device in Fig. 3b shows the detailed structure composed of electrode layer and solid-state electrolyte film. It proves that the electrolyte is penetrated into the porous electrode, which could enhance the ion exchange. Fig. 3c demonstrates the initial resistance and static water contact angle of porous CNT-PDMS elastomer with different CNT contents. With the CNT content increases, the resistance decreases significantly with the smaller resistivity. Meanwhile, the porous CNT-PDMS elastomer gradually becomes hydrophilic with the CNT content increasing. Then we choose porous CNT-PDMS elastomer with CNT content of 20% as the active material. The infiltration of the electrolyte could be greatly enhanced by the hydrophilic characteristic, which is critical to the electrochemical performance.

To evaluate the electrochemical behavior, the MSC is carefully carried out through cyclic voltammetry (CV), galvanostatic charge-discharge (GCD), and cycling stability measurements via electrochemical workstation at room temperature. At first, CV curves with the scan rates from 10 mV/s to 200 mV/s are recorded at a stable potential window. As shown in Fig. 3d, quasi-rectangular shapes could be observed due to the characteristic of the carbon-based materials, proving the ideal double-layer electrochemical behavior. Then GCD test is also measured in Fig. 3e, where the typical GCD curves are performed, the charging currents of which are from 4 μA to 15 μA. Discharging profiles of the fabricated MSC are dependent on the applied charging-discharging currents. Evidently, the charging curves are nearly symmetrical with their corresponding discharging counterparts, as well as their great linear voltage-time profiles.

Besides, the areal capacitance (C_A) is calculated according to the following equation based on the CV curves with different scan rates:

$$C_A = \frac{Q}{A \cdot \Delta V} = \frac{1}{p \cdot \Delta V} \int_{V_1}^{V_2} I(V) dV \tag{10}$$

where $I(V)$ is the charge–discharge current function, p is the scan rate, A is the area of the MSC and ΔV is the potential window during the discharge process, where V_1 and V_2 are maximum and minimum voltage values, respectively. The MSC could achieve maximum areal capacitance of $249.89\,\mu\text{F/cm}^2$ at the scan rate of 10 mV/s, which decreases slightly with the increase of the scan rate. Taking advantage of porous structure with large surface area and highly conductive elastomer, the MSC demonstrates great electrochemical behavior with reliable areal capacitance.

For the reliability as the energy storage component in flexible electronics, the MSC device is tested under various bending or rolling state at the scan rate of 100 mV/s. From Fig. 3g, there are negligible changes of the CV curves, which proves excellent flexibility of the MSC
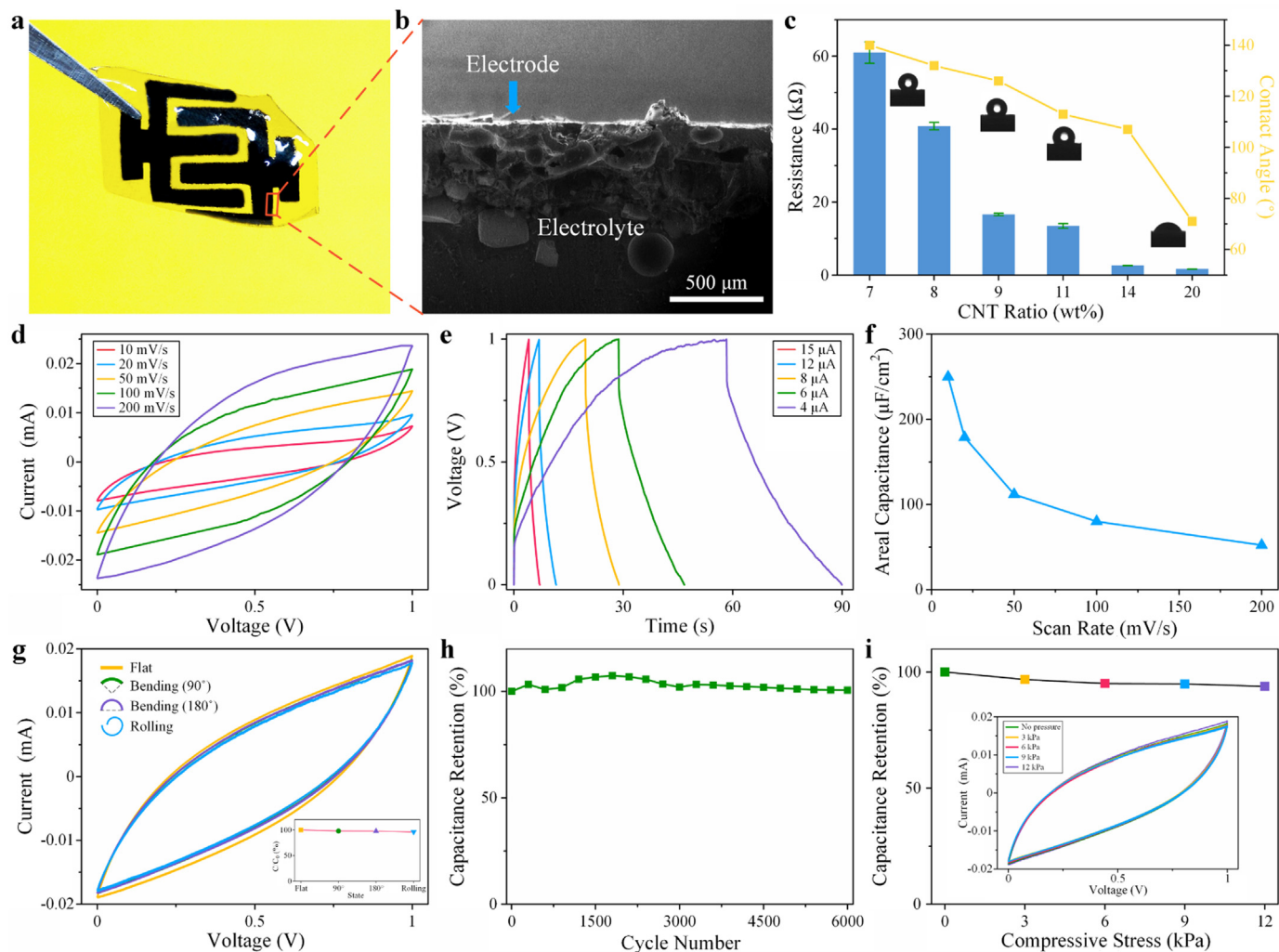
Fig. 3. a) Digital image of flexible MSC device. b) Cross-section view of SEM image of electrode-electrolyte layout. c) Initial resistance and static water contact angle (optical images of water droplets) with different CNT contents. Electrochemical behavior of MSC. d) CV curves at different scan rates, e) GCD curves with different charging/discharging currents, and f) calculated areal capacitance based on CV curves. With scan rate of 100 mV/s, g) CV curves under different bending and rolling states (with inset image showing stable areal capacitance), h) cycling stability after 6000 charging cycles, and i) capacitance retention under different compressive stress (with inset image showing corresponding CV curves).

device. The inset image shows the capacitance retention under different bending conditions, which maintains stably compared to the initial state. As for the cycling stability, Fig. 3h shows the capacitance retention of the MSC device with interdigital electrodes during charging-discharging cycles (100 mV/s). It is obvious that the capacitance of the device increases at the beginning due to the electrode self-activation process. Then it degrades gradually and remains about 100.5% after 6000 cycles compared with initial capacitance. As another crucial metrics for evaluating the capability of energy storage device, the energy density and power density (Ragone plot) is shown in Fig. S7 (Supporting information) compared with other related works, which reveals good capability in delivering energy and satisfying the practical applications.

In addition, when assembled into the sensing patch, the MSC device is required to work reliably under applied stress. Thus, the pressure-tolerant capability is crucial to the device. As shown in Fig. 3i, the device shows no noticeable performance degradation in the CV curves under different applied stress (inset image). The normalized capacitance, calculated from the corresponding CV curves, exhibits high stable performance within a variation of 7% under 12 kPa compared with the initial state. Therefore, owing to the stable electrochemical

performance and desirable mechanical durability, the MSC device shows promising potential in driving PRS for pressure sensing.

3.4. Applications of all-in-one piezoresistive-sensing patch

As mentioned before, it is urgent to develop and integrate flexible energy devices with functional electronics to exert their full potentials in health monitor and safety communication. Assembled with the PRS and MSC through the middle PDMS layer to avoid interference, sensing patch could be achieved with mechanical durability and reliable sensitivity shown in Fig. 4a. Taking advantage of the ultrasensitive PRS with repeatability and negligible variance of the MSC under mechanical deformation, such sensing patch could power itself, which shows promising applications in movement detection and signal recognition.

When the MSC unit is charged, resistance of PRS (R_X) could be calculated through the voltage signal of the constant resistance according to the circuit diagram (inset of Fig. 1a) as follows:

$$R_X = \left(\frac{V_C}{V_P} - 1\right) \cdot R_P \tag{11}$$

where R_P represents the constant resistance, V_C and V_P represent the
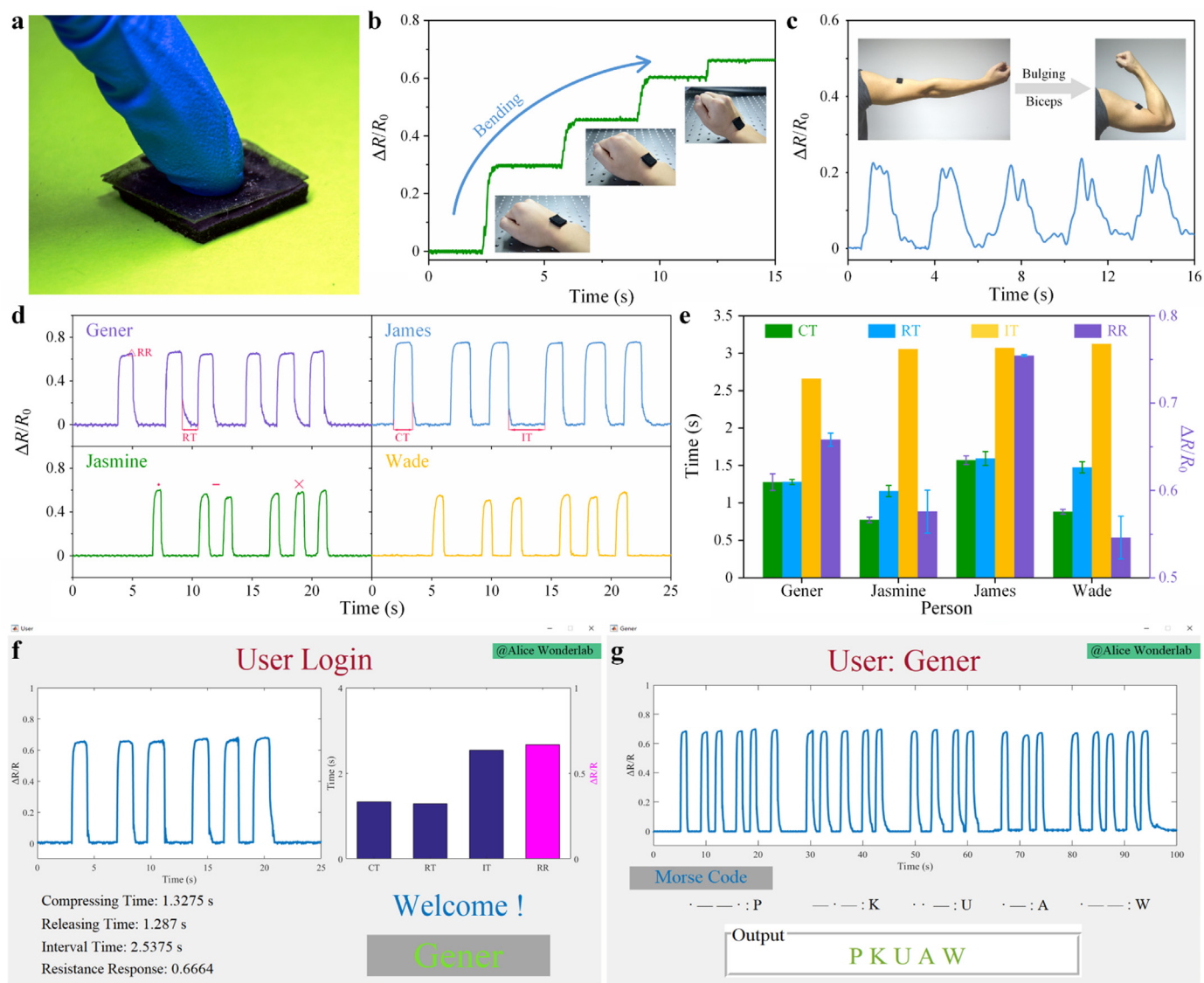
Fig. 4. All-in-one sensing patch for health monitoring and safety communication. a) Digital photograph of the sensing patch touched by a finger as the 3D touch. Digital images and corresponding resistance response of the sensing patch attached among the b) wrist and c) arm to monitor the joint and muscle movements. d) Recorded resistance responses of 3D touch with four persons during the same compressing processes, one touch for "·", two touches for "−", and three touches for "×". e) Feature parameters extraction from four curves, such as compressing time, releasing time, interval time and resistance response. 3D touch for user identification and safety communication as human-machine interface. f) Login program through recorded resistance response with feature parameters matching and user identification. g) Decoding of Morse code from the resistance response after the specific user login for safety communication.

voltage of the MSC and the R_P, respectively. Obviously, the resistance response is determined by the relative magnitude of voltage of the constant resistance to the voltage of MCS, instead of the absolute value of the MSC. To effectively extend the operating time, we utilize the constant resistance with high resistance (1 MΩ) and the total dischar-ging current in the circuit diagram is less than 1 μA. While the charged MSC drives the PRS, the PRS could operate stably more than 130 s as shown in the Fig. S8 (Supporting information).

In detail, our piezoresistive-sensing patch attached on the wrist could clearly identify the hand motion, which exerts stable resistance response in accordance to the joint bending state. The resistance re-sponse could further increase with the enlargement of the bending angles (Fig. 4b). After attached on the arm near the biceps, the sensing patch oscillates resistance responses synchronously with the periodic movements of the muscle. When the muscle contraction motions are repeated, the compressive strain is applied as indicated with the re-sistance response shown in Fig. 4c. These stable responses of both joint

and muscle movements confirm the satisfactory capability of the sen-sing patch to distinguish different-scale strains.

In addition, the piezoresistive-sensing patch could be utilized as the self-driven 3D touch with the high sensitivity and mechanical robust-ness in the user identification and safety communication. Fig. S9 (Supporting information) shows data flow chart of the human-machine interface, which contains an oscilloscope, a laptop computer, cables and the sensing patch. When the finger compresses the sensing patch, the resistance response could be recorded in oscilloscope and transmitted into the laptop for further processing. At first, several persons are re-quired to touch the sensing patch in the specific means divided into three groups, where one touch represents "·", two touches represent "−", and three touches represent "×", respectively. According to the recorded re-sistance response curves in Fig. 4d, we define the maximum signal data as resistance response (RR), the touching time with the sensing patch as the compressing time (CT), the non-contact time as the releasing time (RT) and the interval between two touch groups as the interval time (IT), respectively.
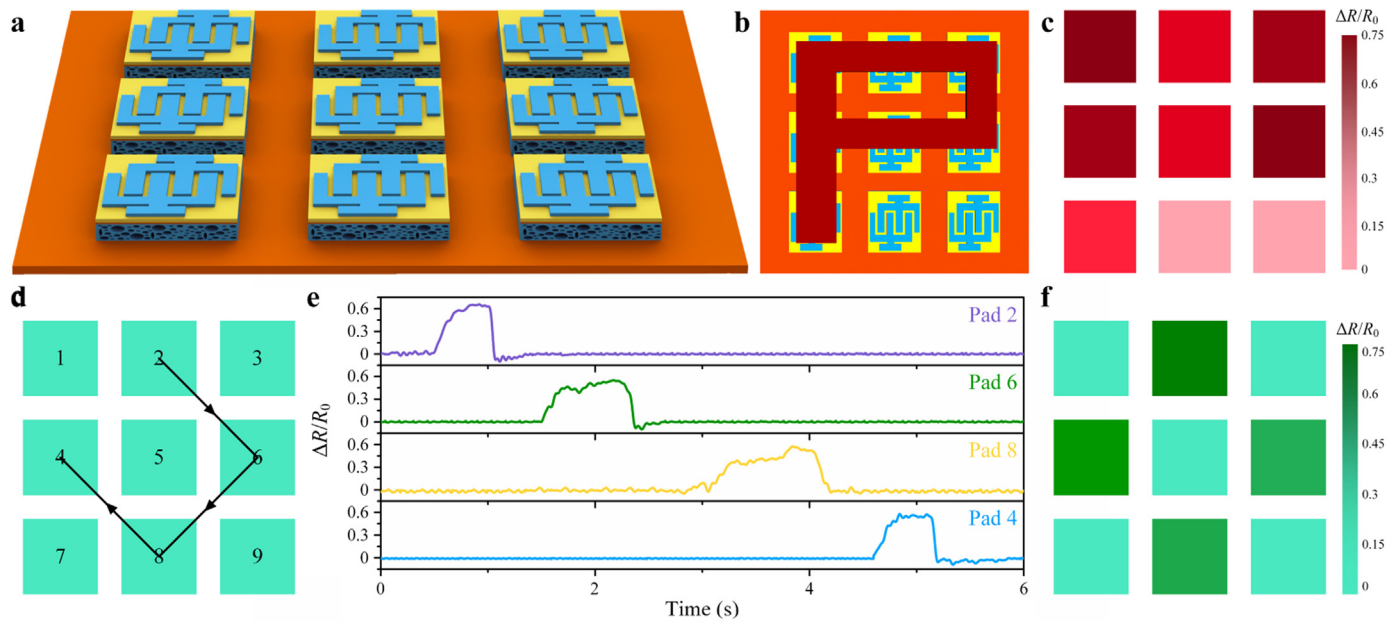
Fig. 5. Static pressure sensing and dynamic tactile trajectory of sensing patch matrix. a) Schematic diagram of the 3 × 3 multiple-pixel smart patch matrix. b) The sensing patch matrix loaded by a "P" character-shape acrylic plate and c) corresponding resistance signals of the 9 pixels. d) Illustration of the trajectory of finger movement over the smart patch matrix. e) Recorded resistance response and f) corresponding tactile trajectory of the passed pads.

Then the corresponding feature parameters of each person could be extracted as shown in Fig. 4e. Obviously, due to the different touching habit of each person, it could be separated easily through the comparison of feature parameters, which shows possibility in user identification and login program. Thus, when we input a new command at the specific means, the corresponding feature parameters could be extracted as shown in MATLAB software interface (Fig. 4f). Through the parameter comparison, the user "Gener" matches whole features, who could successfully login the program. After login, the user further inputs the communication information by touching the sensing patch with different sequence. By judging the number and interval time of the touching process, the recorded resistance responses could be decoded into corresponding characters through the Morse code. As shown in Fig. 4g, in the communication interface, the output of specific user is safely decoded into five characters, "PKUAW". Therefore, a novel approach in human-machine interface, the sensing patch as 3D touch for user identification and safety communication, is successfully developed, thus showing a broad perspective in potential applications.

To measure the feasibility of pressure sensing and tactile trajectory, sensing matrix of 9 pixels (3 × 3 sensing patch units) is fabricated among the PDMS substrate, which is schematically illustrated in Fig. 5a. The sensing matrix identifies not only the different weight of pieces but also the corresponding position according to the different resistance response intensity. When a "P" character-shape acrylic plate is placed among the sensing matrix (Fig. 5b), resistance responses could literally represent the touch area and corresponding distributed weight (Fig. 5c). When the "PKU" character-shape acrylic plates are successively placed among the sensing matrix shown in Fig. S10 (Supporting information), we could rebuild the 3D character on the corresponding position in accordance with the column height. This capability to identify the stress distribution meets the demand of static pressure sensing.

As for the capability to realize spatially resolved tactile trajectory, mapping figure of pressure distributions is constructed. When the index finger moves along the sensing matrix, as depicted in Fig. 5d, real-time mapping of finger tactile trajectory could be recorded. The corresponding pads will exert resistance response intensity, during which time, the sliding velocity and compressing time of the passed pad could be further detected (Fig. 5e). Through reading the color shades of the sensing matrix with different stress intensity, the tactile trajectory could

be straightforwardly identified shown in Fig. 5f. Therefore, the dynamic tactile trajectory of the finger motion can be imaged in addition to pressure distribution.

4. Conclusion

In summary, we have proposed an all-in-one sensing patch integrated with piezoresistance sensor and micro-supercapacitor based on the porous CNT-PDMS elastomer, which owns mechanical durability and electrical stability. As the functional fraction, the PRS exhibits high sensitivity and reliable capability in monitoring various stress, the mechanical performance of which could be further modulated by the CNT content and pore size. As for the energy storage fraction, the MSC is configured with porous CNT-PDMS elastomer as active materials, PVA/H_3PO_4 as substrate and solid-state electrolyte, which shows reliable areal capacitance and cycling stability, attributed to the fact that porous elastomer possesses large surface area and high conductivity. By assembling the PRS with MSC, sensing patch could be attached among human body to monitor both joint and muscle movements through the resistance responses. In addition, the piezoresistive-sensing patch could be utilized as a self-driven 3D touch with the high sensitivity and mechanical robustness in user identification and safety communication. After packaged into the sensing matrix, it shows capable of static pressure sensing and dynamic tactile trajectory with accuracy. Therefore, through strategical design and performance optimization, such all-in-one piezoresistive-sensing patch shows promising potentials in smart energy systems and human-machine interfaces.

Appendix A. Supporting information

Supplementary data associated with this article can be found in the online version at doi:10.1016/j.nanoen.2018.08.041.

References

[1] W. Gao, S. Emaminejad, H. Nyein, S. Challa, K. Chen, A. Peck, H. Fahad, H. Ota, H. Shiraki, D. Kiriya, D. Lien, G. Brooks, R. Davis, A. Javey, Nature 529 (2016) 509–514.

[2] Z. Wen, J. Chen, M. Yeh, H. Guo, Z. Lia, X. Fan, T. Zhang, L. Zhu, Z. Wang, Nano Energy 16 (2015) 38–46.

[3] Y. Jie, H. Zhu, X. Cao, Y. Zhang, N. Wang, L. Zhang, Z. Wang, ACS Nano 10 (2016) 10366–10372.

[4] X. Wang, Y. Yin, F. Yi, K. Dai, S. Niu, Y. Han, Y. Zhang, Z. You, Nano Energy 39 (2017) 429–436.

[5] Y. Song, J. Zhang, H. Guo, X. Chen, Z. Su, H. Chen, X. Cheng, H. Zhang, Appl. Phys. Lett. 111 (2017) 073901.

[6] J. Chen, Y. Huang, N. Zhang, H. Zou, R. Liu, C. Tao, X. Fan, Z. Wang, Nat. Energy 1 (2016) 16138.

[7] X. Zhang, M. Han, B. Meng, H. Zhang, Nano Energy 11 (2015) 304–322.

[8] Y. Song, X. Cheng, H. Chen, J. Huang, X. Chen, M. Han, Z. Su, B. Meng, Z. Song, H. Zhang, J. Mater. Chem. A 4 (2016) 14298–14306.

[9] F. Zhang, M. Wei, V. Viswanathan, B. Swart, Y. Shao, G. Wu, C. Zhou, Nano Energy 40 (2017) 418–431.

[10] Y. Song, X. Cheng, H. Chen, M. Han, X. Chen, J. Huang, Z. Su, H. Zhang, Micro Nano Lett. 11 (2016) 586–590.

[11] W. Liu, Z. Chen, G. Zhou, Y. Sun, H.R. Lee, C. Liu, H. Yao, Z. Bao, Y. Cui, Adv. Mater. 28 (2016) 3578–3583.

[12] J. Kim, M. Lee, H. Shim, R. Ghaffari, H. Cho, D. Son, Y. Jung, M. Soh, C. Choi, S. Jung, K. Chu, D. Jeon, S. Lee, J. Kim, S. Choi, T. Hyeon, D. Kim, Nat. Commun. 5 (2014) 5747.

[13] Z. Zhu, R. Li, T. Pan, Adv. Mater. 30 (2018) 1705122.

[14] J. Zhao, N. Li, H. Yu, Z. Wei, M. Liao, P. Chen, S. Wang, D. Shi, Q. Sun, G. Zhang, Adv. Mater. 29 (2017) 1702076.

[15] B. Hwang, J. Lee, T. Trung, E. Roh, D. Kim, S. Kim, N. Lee, ACS Nano 9 (2015) 8801–8810.

[16] J. Yun, Y. Lim, G. Jang, D. Kim, S. Lee, H. Park, S. Hong, G. Lee, G. Zi, J. Ha, Nano Energy 19 (2016) 401–414.

[17] Y. Song, H. Chen, Z. Su, X. Chen, L. Miao, J. Zhang, X. Cheng, H. Zhang, Small 13 (2017) 1702091.

[18] L. Dhakar, P. Pitchappa, F. Tay, C. Lee, Nano Energy 19 (2016) 532–540.

[19] Z. Lou, S. Chen, L. Wang, R. Shi, L. Li, K. Jiang, D. Chen, G. Shen, Nano Energy 38 (2017) 28–35.

[20] K. Lee, J. Lee, G. Kim, Y. Kim, S. Kang, S. Cho, S. Kim, J. Kim, W. Lee, D. Kim, S. Kang, D. Kim, T. Lee, W. Shim, Small 13 (2017) 1700368.

[21] M. Liu, X. Pu, C. Jiang, T. Liu, X. Huang, L. Chen, C. Du, J. Sun, W. Hu, Z. Wang, Adv. Mater. 29 (2017) 1703700.

[22] E. Roh, H. Lee, D. Kim, N. Lee, Adv. Mater. 29 (2017) 1703004.

[23] S. Gong, W. Schwalb, Y. Wang, Y. Chen, Y. Tang, J. Si, B. Shirinzadeh, W. Cheng, Nat. Commun. 5 (2014) 3132.

[24] M. Amjadi, A. Pichitpajongkit, S. Lee, S. Ryu, I. Park, ACS Nano 8 (2014) 5154.

[25] Z. Chen, C. Xu, C. Ma, W. Ren, H.M. Cheng, Adv. Mater. 25 (2013) 1296.

[26] H. Chen, L. Miao, Z. Su, Y. Song, M. Han, X. Chen, X. Cheng, D. Chen, H. Zhang, Nano Energy 40 (2017) 65–72.

[27] X. Wu, Y. Han, X. Zhang, Z. Zhou, C. Lu, Adv. Funct. Mater. 26 (2016) 6246–6256.

[28] H. Chen, Z. Su, Y. Song, X. Cheng, X. Chen, B. Meng, Z. Song, D. Chen, H. Zhang, Adv. Funct. Mater. 27 (2017) 1604434.

[29] C. Boland, U. Khan, G. Ryan, S. Barwich, R. Charifou, A. Harvey, C. Backes, Z. Li, M. Ferreira, M. Möbius, R. Young, J. Coleman, Science 354 (2016) 1257–1260.

[30] X. Lu, M. Yu, G. Wang, Y. Tong, Y. Li, Energy Environ. Sci. 7 (2014) 2160–2181.

[31] K. Wang, W. Zou, B. Quan, A. Yu, H. Wu, P. Jiang, Z. Wei, Adv. Energy Mater. 1 (2011) 1068–1072.

[32] M. Beidaghi, Y. Gogotsi, Energy Environ. Sci. 7 (2014) 867.

[33] D. Zhao, C. Chen, Q. Zhang, W. Chen, S. Liu, Q. Wang, Y. Liu, J. Li, H. Yu, Adv. Energy Mater. 7 (2017) 1700739.

[34] D. Kim, D. Kim, H. Lee, Y. Jeong, S. Lee, G. Yang, H. Kim, G. Lee, S. Jeon, G. Zi, J. Kim, J. Ha, Adv. Mater. 28 (2016) 748–756.

[35] B. Xie, Y. Wang, W. Lai, W. Lin, Z. Lin, Z. Zhang, P. Zou, Y. Xu, S. Zhou, C. Yang, F. Kang, C. Wong, Nano Energy 26 (2016) 276–285.

[36] Y. Song, X. Chen, J. Zhang, X. Cheng, H. Zhang, J. Microelectromech. Syst. 26 (2017) 1055–1062.

[37] M. El-Kady, R. Kaner, Nat. Commun. 4 (2013) 1475.

[38] S. Pyo, J. Lee, M. Kim, T. Chung, Y. Oh, S. Lim, J. Park, J. Kim, J. Micromech. Microeng. 24 (2014) 075012.

[39] H. Yao, J. Ge, C. Wang, X. Wang, W. Hu, Z. Zheng, Y. Ni, S. Yu, Adv. Mater. 25 (2013) 6692.

[40] J. Kuang, Z. Dai, L. Liu, Z. Yang, M. Jin, Z. Zhang, Nanoscale 7 (2015) 9252.

[41] Y. Wu, H. Liu, S. Chen, X. Dong, P. Wang, S. Liu, Y. Lin, Y. Wei, L. Liu, ACS Appl. Mater. Interfaces 9 (2017) 20098.

[42] Q. Chen, P. Cao, R. Advincula, Adv. Funct. Mater. 28 (2018) 1800631.